Understanding the microstructural evolution of hypersaline cemented paste backfill with low-field NMR relaxation

Razyq Nasharuddin,[a] Ganhua Luo,[b] Neil Robinson,[a] Andy Fourie,[b] Michael L. Johns,[a] and Einar O. Fridjonsson[a]*

[a] *Department of Chemical Engineering, The University of Western Australia, 35 Stirling Highway, Crawley, WA 6009, Australia*

[b] *Department of Civil, Environmental and Mining Engineering, The University of Western Australia, 35 Stirling Highway, Crawley, WA 6009, Australia*

*Email: einar.fridjonsson@uwa.edu.au

Abstract

Cemented paste backfill (CPB) comprising mineral tailings, binders and mixing waters is an important potential support material in the mining industry. As the mechanical properties of CPB are significantly influenced by its microstructural characteristics the development of measurement tools to better understand its pore structure evolution is important for its increased utilisation. This study reports the application of low-field nuclear magnetic resonance (NMR) relaxation time measurements to characterise the microstructural evolution of CPB materials over 56 days of hydration, contrasting common tap water and hypersaline water (~22 wt% salt) as mixing waters. Distinct NMR relaxation time populations were evidenced within each CPB sample, revealing the presence of both capillary ($T_{1,2} \approx 10$ ms) and gel pore water ($T_{1,2} \approx$ 300 – 500 μs), with time-dependent relaxation measurements facilitating characterisation of capillary pore structure evolution over the hydration period assessed. Hypersaline samples demonstrated a time-lag in this measured capillary pore evolution, relative to those hydrated with tap water, while pore structure evolution rates were observed to increase with increased CPB binder content. Further, both T_1 and T_2 NMR relaxation times were found to correlate with the uniaxial compressive strength of the CPB materials investigated, facilitating the formulation of a predictive correlation function between NMR relaxation characteristics and mechanical properties.

Keywords

Cemented paste backfill; Tailings Management; Nuclear Magnetic Resonance; Microstructure

Highlights

- Microstructural evolution of CPB, prepared with tap and hypersaline water, is monitored using low-field NMR relaxometry.
- T_1 and T_2 NMR relaxation measurements compared with mechanical strength via UCS tests.
- Hypersaline mixing water results in slower structural evolution and lower mechanical strength.

Introduction

It is estimated that the production rate of mine tailings ranges between 5 and 7 billion tonnes per year worldwide [1]. While mine tailings are often discharged into tailings ponds, the emergence of cemented paste backfill (CPB) technology has the potential to substantially alter and enhance the role of tailings in the mining industry [2]. CPB comprises three main components, namely dewatered mine tailings (70-85 % solids by weight), mixing water and hydraulic binders (3-7 % by paste weight), which may include Ordinary Portland Cement (OPC), fly ash, and ground granulated blast furnace slag; these components combine via hydration reactions to form a complex porous structure which may be utilised as a passive support material within underground mining operations [3].

It is well-known that mixing water chemistry, including acidity and ionic concentrations, can impact the mechanical properties of hydrated CPB materials [2,4]. As access to low-salinity water in many mining operations is limited, and the local source water typically hypersaline, it is therefore of significant interest to determine the influence of hypersaline mixing water on the evolution of hydrated CPB materials. As such, in the present study we compare the effects of hypersaline water (~22 wt% salt) obtained from a Western Australian mine site, combined with mine tailings from the same site, against the effects of tap water on both the microstructural and mechanical strength evolution of the resultant CPB.

A number of recent studies have investigated the relationship between the microstructure of next-generation cementitious materials and the resulting mechanical properties. For example, Burciaga-Diaz *et al*. contrasted the compressive strength of alkali-activated slag pastes with solid state ^{29}Si and ^{27}Al NMR spectroscopy, facilitating quantification of the hydration products formed and their association with material strength [5]. Ma

et al. applied a similar approach to fly ash cement pastes, evidencing compressive strength enhancements which accompany Si/Al substitution reactions within the hydration products in the presence of an organic activator [6]. Fridjonsson *et al*. were the first to monitor the pore size evolution of CPB samples during their hydration using NMR, revealing through the application of nuclear spin relaxation measurements both a reduction in pore size during the hydration process, and a scaling relationship between pore size and material permeability [7]. Sun *et al.* studied the evolution of CPB porosity under uniaxial compression via X-ray CT analysis [8]. This study sequenced CPB failure into four stages, namely (i) a no microcrack region; (ii) initiation and aggregation of microcracks; (iii) connection of microcracks; and (iv) formation of a macroscopic fracture region, and further showed that the CPB materials investigated displayed tensile and shear failures during early and middle-to-late stages of uniaxial compression, respectively. Furthermore Liu *et al.* studied CPB using both NMR and SEM to investigate the relationship between uniaxial compressive strength (UCS) and CPB pore characteristics, observing an exponential decrease in UCS with increasing porosity [9].

In the current study the results of low-field nuclear magnetic resonance (NMR) relaxation measurements are contrasted with UCS analysis to monitor the compressive strength and pore size evolution of CPB samples prepared with both tap and hypersaline mixing waters. A significant advantage of using low-field NMR is that it provides a non-destructive method for the characterisation of porous media [10]. As such, it offers opportunities for the development of robust approaches for monitoring CPB samples under early hydration conditions without the requirements for sample modifications, such as solvent exchange or oven drying, which may damage the material microstructure [11,12]. Indeed, as the longitudinal and transverse NMR relaxation times T_1 and T_2 are both inherently sensitive to molecular dynamics [13], the relaxation characteristics of fluids confined to porous structures can provide unique insight into material structural properties including pore size distributions and pore network connectivity [7,14–21].

Theory

Utilising ^{1}H (proton) relaxation measurements this study considered the dynamics of water confined to the pore structures of the CPB materials. Such systems are assumed to exist under the conditions of biphasic fast exchange, wherein the rates of mixing between water molecules adsorbed at the pore surface and those towards the centre of the pore is considered to be rapid relative to their intrinsic rates of NMR relaxation [22]. Under such conditions the measured relaxation rates T_i^{-1} (with $i = 1$ or 2 for longitudinal or transverse NMR relaxation, respectively) are given by a combination of unrestricted (bulk), surface (adsorbed) and confinement contributions according to [23]

$$\frac{1}{T_i} \approx \frac{1}{T_{i,bulk}} + \frac{2\alpha\rho_i}{d_{pore}} + \frac{8\alpha D}{d_{pore}^2}. \quad (1)$$

Here $T_{i,bulk}$ are the relaxation time constants of the unrestricted fluid, α is a shape parameter which takes values of 1, 2 or 3 for planar, cylindrical or spherical pores, respectively [24], *D* is the self-diffusion coefficient of the confined fluid, and ρ_i are the longitudinal ($i = 1$) and transverse ($i = 2$) surface relaxivities, which define the rates of enhanced NMR relaxation which occurs at the pore surface [17,18,25]. Importantly, d_{pore} is the pore diameter of the confining pore structure; Equation (1) therefore provides a direct link between the observed NMR relaxation time constants and the microstructural characteristics of the materials under investigation. This relationship is further resolved through the assumption of so-called surface-limited relaxation, a regularly-applied assumption for cementitious materials and other heterogeneous porous media, wherein $4D/d_{pore} \gg \rho_i$ [18,19,26,27]. In this case Equation (1) simplifies to [23]

$$\frac{1}{T_i} \approx \frac{1}{T_{i,bulk}} + \frac{2\alpha\rho_i}{d_{pore}}, \quad (2)$$

such that the observed relaxation time constants T_i are proportional to d_{pore}. It follows that the measurement of these time constants throughout the CPB hydration process can provide valuable information on the rates and extent of pore structure evolution, and the influence of different mixing waters on hydration behaviour. Herein we apply this approach to study the pore structure evolution of CPB samples over the first 56 days of hydration, contrasting the behaviour of tap water and hypersaline water hydrated mixtures. We then further investigate the relationship between apparent pore size and material strength characteristics through the comparison of these NMR relaxation times with the results of UCS measurements.

Materials and Methods

Material preparation

Minerals tailings were acquired from the Frog's Leg Gold Mine, located ~19 km west of Kalgoorlie, Western Australia. The tailings were sieved to < 4.75 mm before use to remove any coagulated particles, and dehydrated by drying in air at 110 °C for 24 hours. Figure 1 illustrates the particle size distribution of both the tailings and commercially available slag (sourced from BGC Cement, Australia) used in this study, which were found to exhibit mean (d_{50}) particle sizes of 60 µm and 10 µm, respectively. The chemical composition of the tailings is reported in Table 1 and was assessed by Inductively Coupled Plasma-Optical Emission Spectroscopy (ICP-OES); the tailings were first dried and finely ground, then fused with 12:22 Norrish Flux (Lithium metaborate / Lithium tetraborate) in platinum crucibles at 1050 °C to form glass beads. The beads were then dissolved in 1 M hydrochloric acid, with the resulting solution analysed using an Optima 5300 DV ICP-OES. The detected elemental concentrations were converted to oxide wt% values based on the corresponding atomic weights.

The CPB binders comprised a mixture of slag and OPC in a 2:1 ratio by mass. As cement concentrations used in typical mine sites vary between 1 and 10 wt% we opted here to explore two different binder concentrations exhibiting 5 and 9 wt% binder content, respectively, relative to the total tailings and binder mass; a total solids content of 76 wt% was maintained across all CPB samples investigated. Common tap water and hypersaline water were used as mixing waters, with the hypersaline water obtained from the same site as the mineral tailings. Chemical analysis of these waters was conducted via ICP-OES and anion chromatography, with the resulting ionic composition data reported in Table 2. Anion chromatography tests were conducted using a Thermo Scientific Dionex IonPac AS23 instrument while cation concentrations were obtained using an Optima 5300 DV ICP-OES.

To form the CPB samples the dehydrated tailings and hydraulic binders were mixed with either tap water or hypersaline water for 3 minutes at 90 rpm using a stand mixer. The resultant CPB pastes were subsequently transferred to cylindrical plastic moulds (diameter = 50 mm, height = 100 mm) for UCS analysis, and to cylindrical plastic containers (diameter = 44 mm, height = 108 mm) for NMR analysis; the samples were each cured at 20 ± 2 °C with a relative humidity of 95 % until the appropriate hydration time was attained.

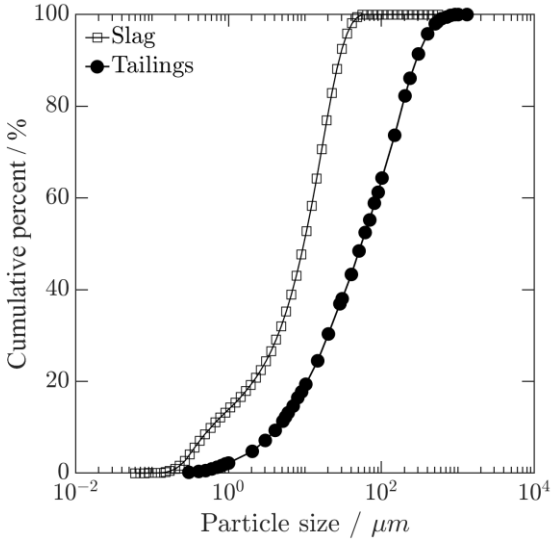

Figure 1: Particle size distributions of tailings and slag. Tailings exhibit d_{60} ~ 90 μm, d_{50} ~ 60 μm and d_{10} ~ 5 μm, while the slag exhibits d_{60} ~ 13 μm, d_{50} ~ 10 μm, and d_{10} ~ 0.6 μm. Prior to analysis both the tailings and slag were pre-screened to remove large rocks and agglomerates.

Table 1. Chemical composition of the mine tailings used in this study obtained from ICP-OES analysis.

Chemical composition	Content (wt%)	Chemical composition	Content (wt%)
SiO_2	68.49	K_2O	1.34
Al_2O_3	9.55	SO_3	1.13
Na_2O	3.31	TiO_2	0.54
Fe_2O_3	3.18	MnO	0.08
CaO	3.16	P_2O_5	0.05
MgO	1.56		

Table 2. Chemical compositional analysis of the mixing waters used in this study obtained from ICP-OES and anion chromatography.

Hypersaline water / mg L^{-1}		Tap water / mg L^{-1}	
Ca^{2+}	955	Cl^-	620
Fe	<0.002	SO_4^{2-}	6
K^+	230	Br^-	1
Mg^{2+}	7790		
Na^+	61900		
Cl^-	115000		
SO_4^{2-}	4480		
Br^-	199		

Uniaxial compressive strength tests

UCS is a key mechanical property in CPB analysis. The UCS of our CPB samples was measured using an Electro-hydraulic Servo-controlled universal testing machine (GDS LF-50) with a maximum load capacity of 50 kN. Tests were conducted once the CPB samples had been cured for 7, 14, 28 and 56 days. Following each curing process the CPB samples were placed between two parallel plates and were loaded under constant displacement conditions with a displacement rate of 1 mm min^{-1}. UCS readings were recorded every second and the axial loading terminated when the sample developed an obvious shearing plane. Tests were performed in triplicate with the average of the three values reported here; a maximum 10% standard deviation from the mean strength was observed across all samples.

High resolution X-ray computed tomography

X-ray µ-CT was performed to obtain an estimate of the (capillary) pore size distribution of CPB materials. A single material sample comprising 5 wt% binder was prepared in a glass vial (diameter = 5 mm, height = 25 mm) and scanned using a Zeiss XRM520 3D X-ray microscope with a 1 µm voxel resolution. A total of 1600 projections were recorded over 360° (i.e. 0.225° rotation of the sample between each projection). Artefacts were either reduced during acquisition or corrected during the reconstruction procedure, and image filtering was performed using a non-local mean algorithm which acted to enhance the image by reducing noise and improving phase discrimination. Segmentation into different phases (pores and solids) was achieved using a modified version of the 3D gradient watershed algorithm, attributing a range of grayscale values to a given phase, with phase boundaries being located at the point of maximum gradient in grayscale, as described elsewhere [28]. Each reconstructed dataset was processed using Avizo 9.5 (ThermoFisher) and MATLAB (MathWorks Inc.) according to the workflow described in [28].

Nuclear magnetic resonance relaxation measurements

NMR relaxation experiments were conducted using a benchtop Magritek Rock Core Analyser equipped with a 0.05 T cylindrical Halbach magnet array, providing a ^{1}H NMR frequency of 2 MHz. The radio frequency (RF) pulse lengths were fixed at 20 µs with the pulse amplitudes for 90° and 180° RF pulses set to -12.5 dB and -6.5 dB, respectively. Both the longitudinal (T_1) and transverse (T_2) nuclear spin relaxation characteristics of our CPB materials were measured, with the RF pulse sequences used illustrated in Figure 2. Measurements were

performed on each day for two weeks (days 1 – 14) followed by further analysis on days 28, 30, 31 and 56. All NMR measurements were performed with a constant magnet bore temperature of 30 °C. Both T_1 and T_2 measurements were performed using a recycle delay of 10 s and 4 repeat scans, resulting in acquisition times of 15 minutes and 1 minute, respectively, and signal-to-noise ratios > 200.

Longitudinal relaxation times were measured using the standard inversion-recovery (IR) pulse sequence shown in Figure 2a [29]. Starting from thermal equilibrium wherein the sample magnetisation lies parallel to the external magnetic field (conventionally the z-axis), the IR measurement is initiated by a 180° RF pulse which rotates the sample magnetisation onto the -z axis. Longitudinal relaxation processes are then permitted for a variable recovery period τ_1 during which the sample magnetisation recovers towards equilibrium. Following each recovery period a 90° RF pulse acts to rotate the magnetisation into the transverse plane, allowing the magnitude of the sample magnetisation to be measured [30]. In this work 20 logarithmically-spaced τ_1 recovery times between 0.5 ms and 500 ms were used. The resulting longitudinal relaxation data are described according to a Fredholm integral equation of the first kind [31],

$$\frac{S(\tau_1)}{S(\tau_1 \to \infty)} = \int K_1(\tau_1, T_1)\, f(T_1)\, d\log_{10}(T_1) + \varepsilon(\tau_1). \quad (3)$$

Here $S(\tau_1)/S(\tau_1 \to \infty)$ is the normalised NMR signal intensity following each τ_1 delay, the Kernel function $K_1(\tau_1, T_1) = 1 - 2\exp(-\tau_1/T_1)$ describes the expected form of T_1 relaxation following the IR experiment [29], and $f(T_1)$ represents the distribution of T_1 time constants present; $\varepsilon(\tau_1)$ is the experimental noise, assumed Gaussian in shape with zero mean.

Transverse relaxation times were measured using the standard CPMG (Carr-Purcell-Meiboom-Gill) experiment shown in Figure 2b [32,33]. Starting again from thermal equilibrium the sample magnetisation is excited into the transverse plane via a 90° RF pulse, which initiates transverse dephasing of the system's magnetic moments. A series of n 180° RF pulses refocusses dephasing arising from inhomogeneity of the static magnetic field, generating a train of n spin echoes which decay according to T_2. In this work we employed $n = 500$ echoes separated by an echo time of $t_e = 100$ μs; this short echo time, together with the low static magnetic field strength employed in this study, aimed to limit the influence of undesired transverse relaxation phenomena due

to magnetic susceptibility contrast effects at the solid-liquid interface [21,34]. The resulting relaxation data are again described by a Fredholm integral equation of the first kind [31],

$$\frac{S(nt_e)}{S(0)} = \int K_2(nt_e, T_2) f(T_2)\, d\log_{10}(T_2) + \varepsilon(nt_e). \quad (4)$$

Here $S(nt_e)/S(0)$ is the normalised NMR signal intensity acquired during each echo, the Kernel function $K_2(nt_e, T_2) = \exp(-nt_e/T_2)$ describes the expected form of T_2 relaxation [33] and $\varepsilon(nt_e)$ again represents the experimental noise.

The desired time constant distributions $f(T_1)$ and $f(T_2)$ were obtained via a numerical inversion of our acquired experimental data according to Equations (3) and (4); as this is an ill-posed problem it was necessary to employ Tikhonov regularisation [35] to ensure the stability of the resulting T_1 and T_2 distributions in the presence of experimental noise, with the smoothing parameter chosen according to the generalised cross-validation method [36]. This robust mathematical inversion technique makes no assumptions about the shape of the resultant probability distributions, and has been successfully implemented across a range of NMR data analysis protocols, including relaxation time distributions in porous media [7,37,38] and droplet sizing methods [39]. The inversion algorithm used in this work was written in MATLAB (MathWorks Inc.) and first used by Griffith *et al*.. [40] As indicated by Equations (3) and (4), as the NMR relaxation time constants exhibited by fluids confined to heterogeneous porous materials are regularly found to vary across multiple decades within the µs – s range, such expression are typically inverted on a logarithmic – rather than a linear – scale [41].

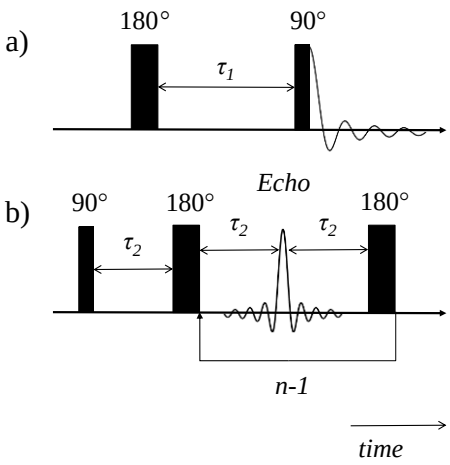

Figure 2. Radio frequency (RF) pulse sequence diagrams for a) T_1 relaxation time measurements via the inversion recovery experiment, and b) T_2 relaxation time measurements via the CPMG experiment. Vertical bars represent RF pulses of constant length; τ_1 represents the variable recovery delays used in the inversion recovery experiment while the CPMG echo time is $t_e = 2\tau_2$.

Results and Discussion

Initial characterisation

Figure 3 illustrates the influence of binders (cement and slag) on the observed T_1 relaxation time distributions of water-saturated tailings. Clearly, when tailings are mixed with either tap or hypersaline water the T_1 distributions appear similar, with dominant peaks located at approximately 15 – 20 ms; this T_1 population is readily assigned to water constricted within the inter-particulate region of the tailings. The addition of 5 wt% binder has a perceivable effect on the observed T_1 distribution, however, and in the case of tap water reduces the dominant T_1 population to ~10 ms. This value is consistent with previous low-field relaxation studies of cementitious systems, which observed T_1 times of this order to correlate with the water population of capillary pore spaces [18,42]. Figure 4 demonstrates CPB pore structure characterisation via high-resolution X-ray µ-CT analysis of a sample containing 5 wt% solids hydrated with tap water for 21 days. This data demonstrates the typical pore size distribution exhibited by such structures, wherein the observed pore spaces are largely present across the length scale 5 – 25 µm. Given the resolution of this µ-CT analysis and the resultant pore size distribution, these structures are readily identified as capillary-type pores.

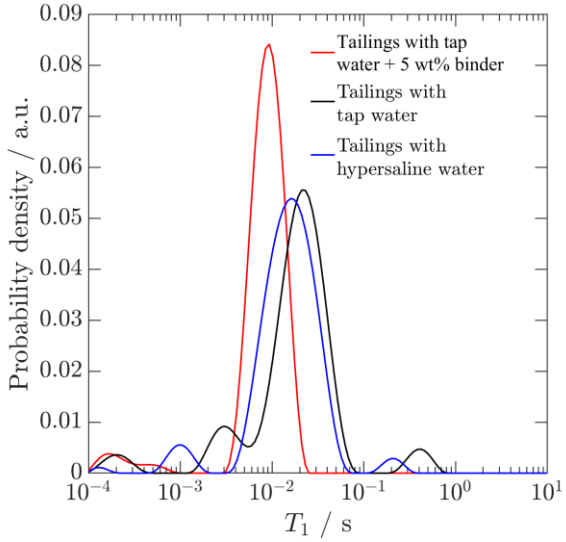

Figure 3. T_1 relaxation time distributions for tap water and hypersaline water saturated tailings samples, and tap water saturated tailings with 5 wt% binder content. A shift to lower T_1 values is evident upon the addition of cement to the sample.

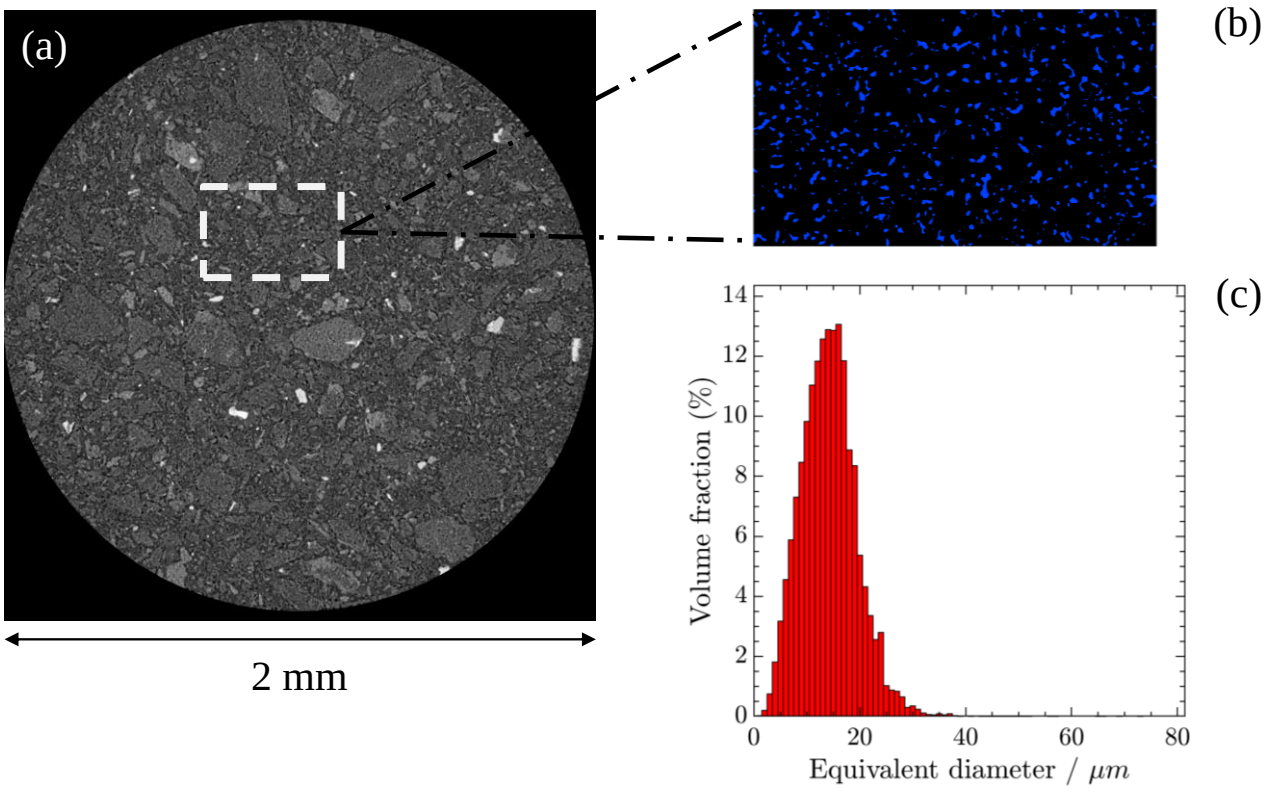

Figure 4. a) X-ray µ-CT image of cemented paste backfill comprising 5 wt% binder content and 76 wt% solids content following hydration with tap water for 21 days. b) Example segmented X-ray µ-CT data identifying the solids (black) and pore space (blue). c) Equivalent pore diameter distribution obtained from the segmentation of image data in a), indicating that observable pores are dominant at the $d_{pore} = 5 – 25$ µm length scale; these are assigned to capillary pore structures.

Pore structure evolution

Figures 5 and 6 report the acquired NMR relaxation data from our CPB materials. Figure 5 illustrates the T_1 and T_2 relaxation time distribution evolution of CPB samples with 5 wt% binder content; Figure 5a and 5b reports the evolution of hypersaline water hydrated CPB, while Figure 5c and 5d reports the evolution following hydration with tap water. In all cases a dominant relaxation peak is observed, which decreases in value over the hydration time scale. In our T_1 data these dominant peaks are initially observed at $T_1 \approx 10$ ms and decrease to $T_1 \approx 2$ ms after 56 days of hydration. As introduced previously, this initial dominant T_1 population can be assigned to water confined within the capillary pore space of the cementitious matrices, [42] which for our CPB materials is expected to occur over the 5 – 25 μm size range (Figure 4). The corresponding T_2 data is displayed in Figure 5b and 5d, wherein the dominant peaks decrease from $T_2 \approx 6$ ms to $T_2 \approx 2$ ms after 56 days. The observation of reduced T_2 values, relative to the T_1 characteristics exhibited by the same porous structure, is in accordance with the known surface relaxation behaviour of fluids confined to cement-based materials [18].

Three distinct T_2 populations are evident at the onset of the hydration process in both the hypersaline water and tap water systems; given our knowledge of the relationship between material pore size and NMR relaxation times (Equation (2)) these peaks may be assigned to distinct water populations occupying pore structures of different sizes. In particular, given the established pore hierarchy of cementitious materials, we assign these populations to capillary pore ($T_2 \sim$ 3-100 ms), interhydrate pore ($T_2 \sim$ 0.8-2 ms) and gel pore ($T_2 \sim$ 300-500 μs) structures, in order of decreasing T_2. This expected pore hierarchy is illustrated in Figure 7 [42–44]. No clear relaxation contributions are observed from solid ^{1}H-bearing hydration products [45], or from water within the associated interlayer spaces [46]; we attribute this absence to the very short T_2 characteristics expected from such features, the measurement of which is likely beyond the echo time limitations of our NMR hardware.

As the hydration processes progress, the interhydrate and capillary pore T_2 populations can be seen to merge, indicating that the capillary and interhydrate pore structures become indistinguishable in the latter stages of CPB hydration. This observation, together with the clear decrease in modal T_1 and T_2 relaxation times within increasing hydration period, is consistent with the known physical mechanisms of cement hydration, whereby hydration products forming at the surface of cement particles ingress into the capillary pore space [47].

No interhydrate water population is observed within the T_1 data presented in Figures 4a and 4b, suggesting such measurements are unable to distinguish between water within capillary and interhydrate pores, even at short hydration times. This observation is consistent with the temporally averaged nature of T_1 measurements, relative to T_2 analysis [48]; this phenomena facilitates a greater degree of diffusive pore-to-pore exchange during relaxation measurements, resulting in greater T_1 averaging between pores of difference size, and hence reduced pore structure resolution. Notwithstanding these observations, the relative T_2 populations assigned to interhydrate and capillary pores demonstrate that the major peaks within our T_1 and T_2 distributions are dominated by water within the capillary pore structures of the CPB materials under investigation.

Similar to Figure 5, Figure 6 illustrates the T_1 and T_2 relaxation time distribution evolution of CPB samples with 9 wt% binder content; Figure 6a and 6b reports the evolution of hypersaline water-hydrated CPB, while Figure 6c and 6d reports the evolution following hydration with tap water. These distributions again illustrate a major peak which we assign as dominated by water within the capillary pore spaces of the CPB materials, and which tends to shorter relaxation times with increasing hydration period. Our T_1 data again shows two separate populations, with the dominant population decreasing from $T_1 \approx 10$ ms to between 1 ms (tap water) and 2 ms (hypersaline water), depending on the mixing water employed. The T_2 data illustrated in Figure 6b and 6d again shows three separate water populations at short hydration times, which we again assign to capillary, inter-hydrate and gel pore structures within the CPB materials. The capillary and inter-hydrate populations are again observed to merge with increasing hydration time; however, we note that this process occurs at a much earlier stage within the hydration process than observed in the 5 wt% binder CPB data shown in Figure 5. This observation therefore indicates that an increase in cement content facilitates more rapid overall structural evolution of the CPB pore hierarchy.

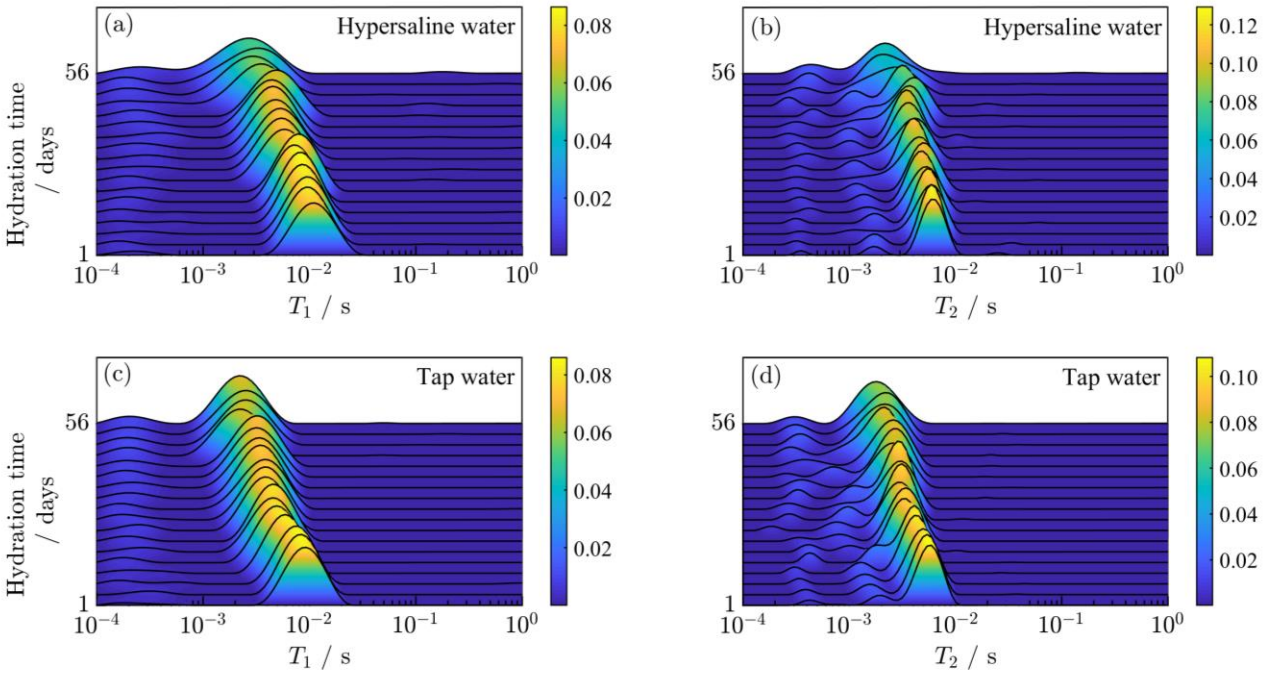

Figure 5. T_1 and T_2 relaxation time distributions for CPB samples comprising 5 wt% binder content and 76 wt% solids. a) and b) illustrate the relaxation distribution evolution when hydrated with hypersaline water, while c) and d) illustrate the corresponding data when hydrated with tap water. Data was acquired on days 1-14, 28, 30, 31 and 56. Colour bars indicate the probability density of the relaxation distributions.

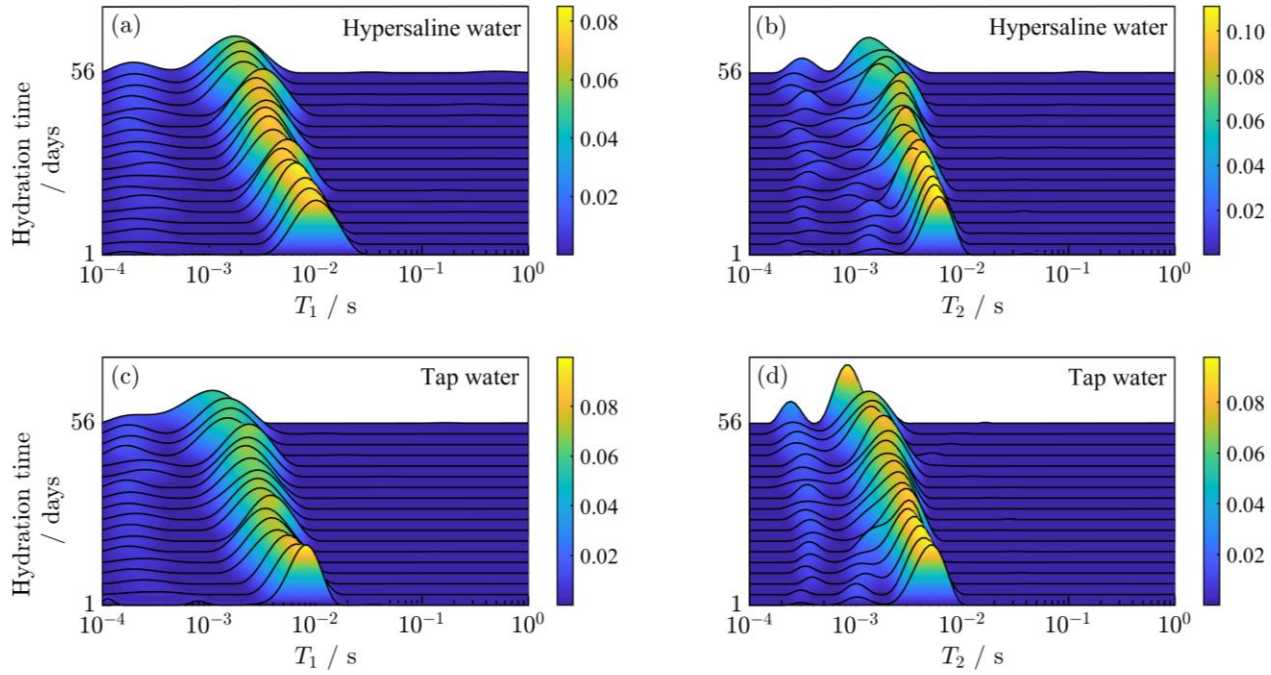

Figure 6. T_1 and T_2 relaxation time distributions for CPB samples comprising 9 wt% binder content and 76 wt% solids. a) and b) illustrate the relaxation distribution evolution when hydrated with hypersaline water, while c) and d) illustrate the corresponding data when hydrated with tap water. Data was acquired on days 1-14, 28, 30, 31 and 56. Colour bars indicate the probability density of the relaxation distributions.

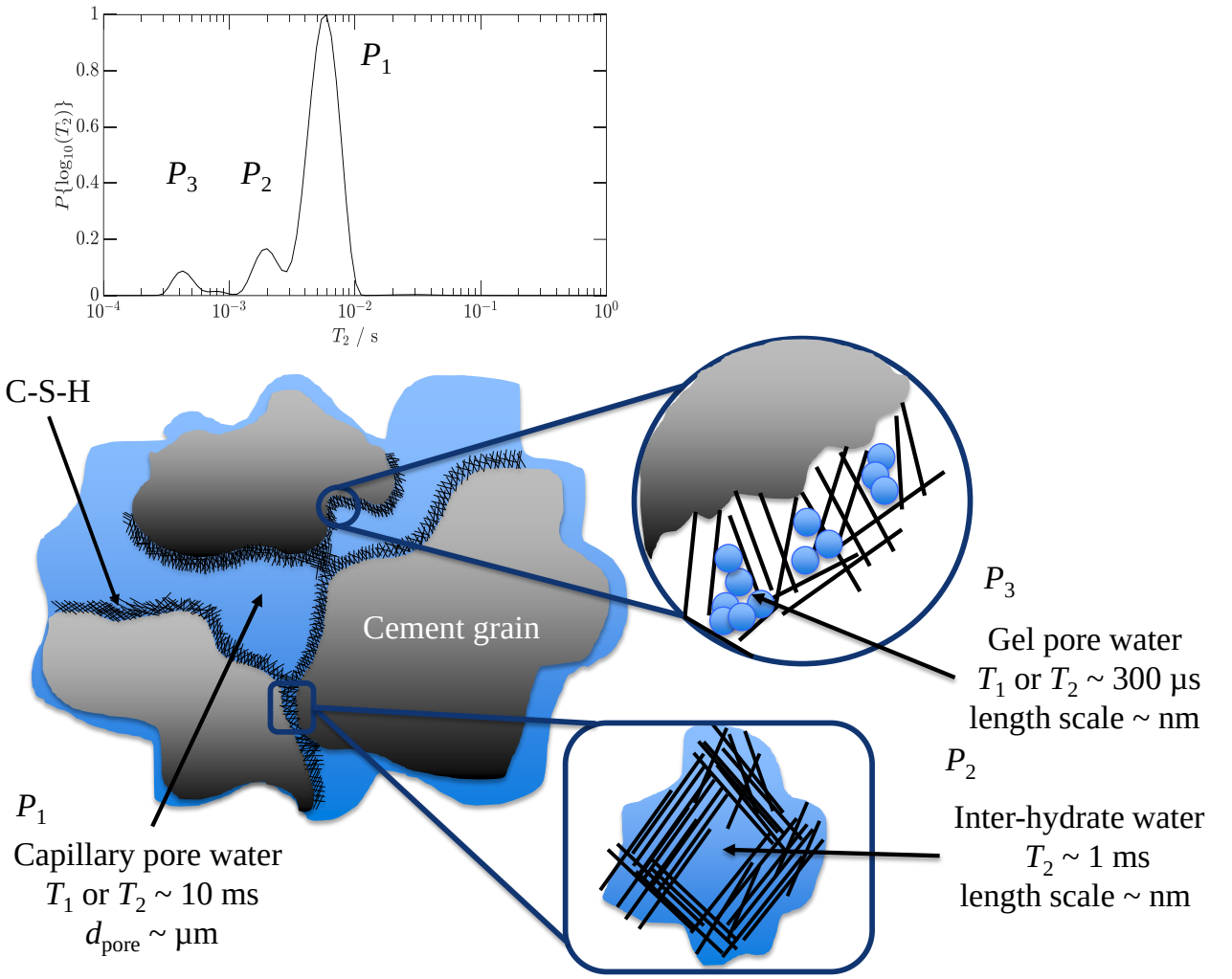

Figure 7: Schematic relating NMR relaxation times T_1 and T_2 to unique water-saturated pore environments in cementitious system. Water in capillary pores exhibit T_1 or T_2 relaxation times of ~ 10 ms, inter-hydrate water display observable T_2 relaxation time of ~ 1 ms, while rapid T_1 and T_2 relaxation times of ~ 300 µs correlate to water in gel pores [42–44]. The abbreviation C-S-H stands for calcium silicate hydrate.

Clearly qualitatively similar trends are exhibited by the eight data sets presented in Figures 5 and 6. This is accentuated in Figure 8 where we consider a quantitative analysis of the modal T_1 and T_2 relaxation times (from here on in referred to as $\langle T_1 \rangle$ and $\langle T_2 \rangle$, respectively) from these distributions as a function of CPB hydration time. As detailed in Figure 8, hypersaline water CPB samples exhibit delayed hydration in terms of $\langle T_1 \rangle$ and $\langle T_2 \rangle$ (suggestive of delayed pore size evolution), relative to the tap water CPB samples. This delay was evaluated by fitting the modal relaxation data to an empirical exponential function of the form

$$\langle T_i \rangle = a_i \exp(-b_i t) + c_i. \quad (5)$$

Here b_i (with i =1 or 2 for T_1 and T_2 measurements, respectively) describes the observed decay rate which characterises the size reduction of the dominant (most populous) pore structure of each sample across the 56 days of hydration assessed, t is the hydration time, while a_i and c_i are a pre-exponential and offset parameters, respectively. The offset parameter c_i is necessary to describe the finite (i.e. non-zero) pore dimensions exhibited by our CPB materials at long hydration times, while the apparent pore sizes at $t = 0$ may be estimated from $(a_i + c_i)$.

The results of the above fitting are detailed in Table 3. The fitted T_1 data suggest that pore structure evolution rates increase upon increasing the binder content from 5 wt% to 9 wt%, consistent with both the rates at which capillary and interhydrate T_2 populations are observed to merge in Figures 5 and 6, and the concept that an increase in binder content should lead to a greater degree of hydration product ingress into the capillary voids; no clear trend emerges from our fitted T_2 data. In terms of comparing the effect of different mixing water we first consider samples containing 5 wt% binder content. Here a decrease in pore structure evolution rate is observed upon moving from tap to hypersaline mixing water within both the T_1 and T_2 data sets, indicating that the use of hypersaline water reduces the overall rate of hydration product ingress into the available capillary voids. Contrasting the behaviour of tap and hypersaline water within samples containing 9 wt% binder content, however, reveals similar decay rates across the two mixing waters; this behaviour is also visibly evident in Figure 8. This finding, together with the above observations concerning increased rates of pore structure evolution in the presence of increased binder content, suggests that the more rapidly developing pore structure hierarchy of the materials containing 9 wt% binder may offset the retardation effects of hypersaline water.

Instead, a clear and persistent difference is observed between the tap water and hypersaline water hydrated CPB data in Figure 8c and d, suggesting that the difference in pore structure (as evidenced via our relaxation measurements) within these materials is dominated by material properties at the initiation of the hydration process.

Table 3: Exponential fitting data of the modal NMR relaxation data illustrated in Figure 8 according to Equation (5). For brevity the rate constant $b_{1,2}$ is given in units of of day^{-1}. Uncertaintly bounds indicate the 95 % confindence intevals obtained from the fitting process.

	$\langle T_1 \rangle$				$\langle T_2 \rangle$			
	a_1 / ms	b_1 / day^{-1}	c_1 / ms	$a_1 + c_1$ / ms	a_2 / ms	b_2 / day^{-1}	c_2 / ms	$a_2 + c_2$ / ms
Tap water 5 wt% binder	8.62 ± 0.84	0.20 ± 0.04	2.44 ± 0.3	11.06 ± 0.90	4.56 ± 0.41	0.18 ± 0.03	2.11 ± 0.19	6.67 ± 0.45
Hypersaline water 5 wt% binder	9.18 ± 0.94	0.12 ± 0.03	2.85 ± 0.60	12.03 ± 1.12	4.31 ± 0.56	0.08 ± 0.03	2.21 ± 0.53	6.52 ± 0.77
Tap water 9 wt% binder	8.26 ± 0.98	0.23 ± 0.05	1.67 ± 0.34	9.93 ± 1.02	4.29 ± 0.31	0.13 ± 0.02	1.14 ± 0.19	5.43 ± 0.36
Hypersaline water 9 wt% binder	9.61 ± 0.88	0.18 ± 0.03	1.98 ± 0.41	11.59 ± 0.97	5.04 ± 0.57	0.13 ± 0.03	1.61 ± 0.36	6.65 ± 0.67

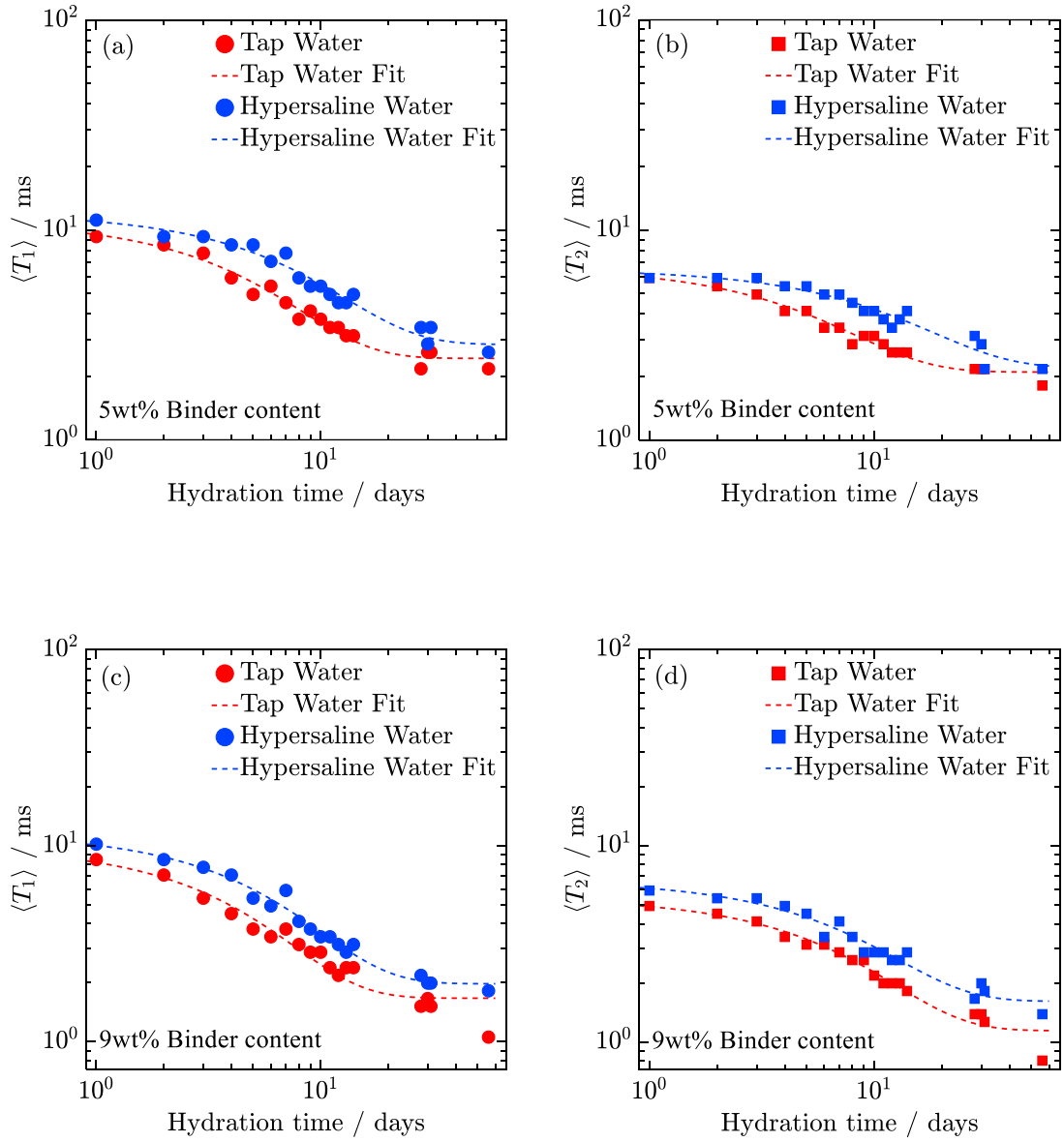

Figure 8: Modal T_1 and T_2 relaxation time data for CPB samples comprising 5 wt% (a and b) and 9 wt% (c and d) binder content and 76 wt% solids as a function of hydration time. Both common tap water (red) and hypersaline water (blue) data is shown in each case. Model fits correspond to Equation (5), with the resulting parameters detailed within Table 3.

NMR relaxation – strength correlations

The mechanical properties of our CPB materials were assessed via uniaxial compressive strength (UCS) analysis; these tests were performed on CPB samples following hydration for 7, 14, 28 and 56 days, providing insight into the mechanical strength of these materials across the range of hydration times examined in our NMR relaxation measurements. UCS analysis on CPB materials experiencing fewer than 7 days of hydration was not possible due to the limited solidification found to have occurred before this time.

Figure 9 details a correlation between the observed $\langle T_1 \rangle$ and $\langle T_2 \rangle$ relaxation times and the results of this UCS analysis, overlaying contributions from both tap water and hypersaline water hydrated CPB materials comprising 5 wt% and 9 wt% binder content. In both data sets there exists a clear trend, with shorter relaxation times correlating with increased mechanical strength. Recalling once again the relationship between NMR relaxation time constants and pore size, these data clearly suggest that CPB materials exhibiting smaller capillary pore structures display comparatively increased mechanical strength characteristics. While there is no clear difference in the UCS results of materials hydrated with tap or hypersaline mixing water at comparative $\langle T_1 \rangle$ or $\langle T_2 \rangle$ times, the lag behaviour of CPB materials hydrated with hypersaline water is clearly apparent within these plots, wherein the hypersaline hydrated CPB is shown to exhibit noticeably reduced UCS load capacities, relative to tap water hydrated CPB of the same age.

Importantly, the two data sets within Figure 9 are described well by an exponential relationship between measured UCS and NMR relaxation characteristics; this relationship takes the form $\mathrm{UCS} = A \exp(-B_i \langle T_i \rangle)$ (with $i = 1$ or 2). Here $A = 1520$ kPa is a pre-exponential load factor which was found to be independent of both the NMR relaxation mechanism probed (T_1 or T_2 relaxation) and the binder content of CPB, while the rate constants take values of $B_1 = 0.459\ \mathrm{s}^{-1}$ and $B_2 = 0.558\ \mathrm{s}^{-1}$ for the $\langle T_1 \rangle$ and $\langle T_2 \rangle$ curves, respectively. The capacity to fit such a simple and predictive expression encompassing the relaxation and mechanical strength properties of both tap water and hypersaline water hydrated CPB materials exhibiting variable binder content is clearly highly desirable; indeed, this expression facilitates the prediction of CPB mechanical strength properties based on the measurement of NMR relaxation times alone. It follows that such correlations provide a potential avenue for the assessment of industrial site CPB formations using NMR logging tools or single sided magnet-based spectrometers [26,49–51].

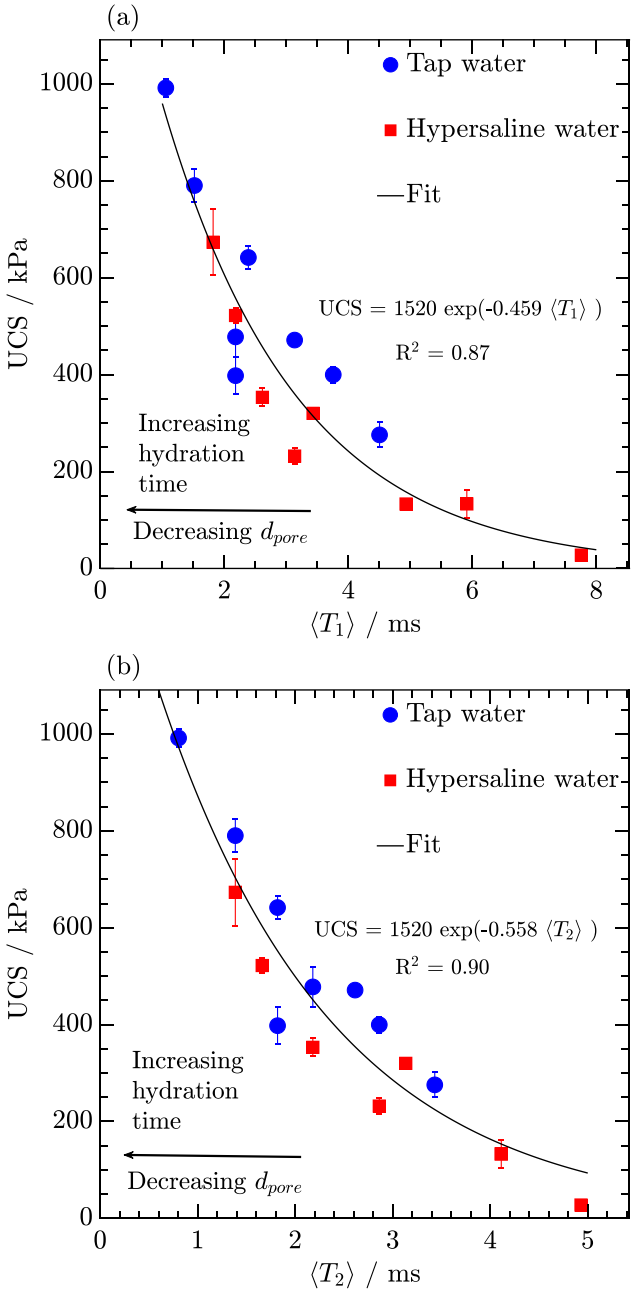

Figure 9: Correlation of a) $\langle T_1 \rangle$ and b) $\langle T_2 \rangle$ NMR relaxation times against CPB UCS data. Data from materials containing both 5 wt% and 9 wt% binder content are overlaid. A model exponential decay is detailed in each case and discussed further in the main text.

Conclusions

Low-field ^{1}H NMR relaxation measurements were utilised to investigate the microstructural characteristics of CPB materials hydrated with both tap and hypersaline mixing waters. Distributions of the NMR relaxation time constants T_1 and T_2 have been demonstrated to provide details on the pore structure hierarchy of such materials, with T_2 data offering resolution between gel, interhydrate and capillary pore structures at short hydration times. These distributions also evidence the time-evolution of CPB capillary pore structures across the first 56 days of hydration. Contrasting the modal NMR relaxation times associated with water confined within these capillary pores provides a non-invasive route with which to quantify and compare the hydration rates of such materials; we demonstrated this approach through both the consideration of different mixing waters and through the comparison of varying binder contents. In general, the use of hypersaline water was observed to reduce CPB capillary pore hydration rates, relative to tap water. Through a direct comparison of NMR relaxation measurements with UCS analysis a predictive correlation has been developed between capillary pore size and mechanical strength, with small pore structures indicative of stronger CPB materials. This correlation is independent of both the NMR relaxation time constants considered and the CPB binder content employed. Furthermore, it highlights a clear lag effect observed in the hydration behaviour of hypersaline hydrated CPB samples, relative to tap water hydrated materials of the same age, resulting in comparatively weaker CPB structures. Overall, this study provides new and unique insight into the microstructural evolution of CPB materials, and highlights distinct relationships between NMR characteristics, pore structure and material strength which may be further exploited in the field through the application of NMR logging tools and single-sided magnets.

Acknowledgement

The authors acknowledge Dr Belinda Godel (CSIRO Minerals Resources) for the high resolution X-ray μCT measurements at the Australian Resources Research Centre (ARRC). Razyq Nasharuddin acknowledges the PhD financial support from the Australian Government Research Training Program (RTP) Scholarship.

Conflicts of Interest

The authors declare that they have no known competing financial interests or personal relationships that could have appeared to influence the work reported in this paper.

References

[1] M. Edraki, T. Baumgartl, E. Manlapig, D. Bradshaw, D.M. Franks, C.J. Moran, Designing mine tailings for better environmental, social and economic outcomes: A review of alternative approaches, J. Clean. Prod. 84 (2014) 411–420. https://doi.org/10.1016/j.jclepro.2014.04.079.

[2] C. Qi, A. Fourie, Cemented paste backfill for mineral tailings management: Review and future perspectives, Miner. Eng. 144 (2019) 106025. https://doi.org/10.1016/j.mineng.2019.106025.

[3] M. Fall, D. Adrien, J.C. Célestin, M. Pokharel, M. Touré, Saturated hydraulic conductivity of cemented paste backfill, Miner. Eng. 22 (2009) 1307–1317. https://doi.org/10.1016/j.mineng.2009.08.002.

[4] D. Deb, T. Sreenivas, G.K. Dey, S. Panchal, Paste Backfill Technology: Essential Characteristics and Assessment of its Application for Mill Rejects of Uranium Ores, Trans. Indian Inst. Met. 70 (2017) 487–495. https://doi.org/10.1007/s12666-016-0999-0.

[5] O. Burciaga-Díaz, J.I. Escalante-García, Structure, mechanisms of reaction, and strength of an alkali-activated blast-furnace slag, J. Am. Ceram. Soc. 96 (2013) 3939–3948. https://doi.org/10.1111/jace.12620.

[6] B. Ma, T. Zhang, H. Tan, X. Liu, J. Mei, H. Qi, W. Jiang, F. Zou, Effect of triisopropanolamine on compressive strength and hydration of cement-fly ash paste, Constr. Build. Mater. 179 (2018) 89–99. https://doi.org/10.1016/j.conbuildmat.2018.05.117.

[7] E.O. Fridjonsson, A. Hasan, A.B. Fourie, M.L. Johns, Pore structure in a gold mine cemented paste backfill, Miner. Eng. 53 (2013) 144–151. https://doi.org/10.1016/j.mineng.2013.07.017.

[8] W. Sun, K. Hou, Z. Yang, Y. Wen, X-ray CT three-dimensional reconstruction and discrete element analysis of the cement paste backfill pore structure under uniaxial compression, Constr. Build. Mater. 138 (2017) 69–78. https://doi.org/10.1016/j.conbuildmat.2017.01.088.

[9] L. Liu, Z. Fang, C. Qi, B. Zhang, L. Guo, K.I.I.L. Song, Experimental investigation on the relationship between pore characteristics and unconfined compressive strength of cemented paste backfill, Constr. Build. Mater. 179 (2018) 254–264. https://doi.org/10.1016/j.conbuildmat.2018.05.224.

[10] J.-P. Korb, Nuclear magnetic relaxation of liquids in porous media, New J. Phys. 13 (2011) 035016. https://doi.org/10.1088/1367-2630/13/3/035016.

[11] J.M. Makar, T. Sato, The effect of drying method on ordinary Portland cement surfaces during the early stages of hydration, Mater. Struct. Constr. 46 (2013) 1–12. https://doi.org/10.1617/s11527-012-9878-2.

[12] J. Zhang, G.W. Scherer, Comparison of methods for arresting hydration of cement, Cem. Concr. Res. 41 (2011) 1024–1036. https://doi.org/10.1016/j.cemconres.2011.06.003.

[13] J. Kowalewski, L. Mäler, Nuclear spin relaxation in liquids: theory, experiments, and applications, 2nd ed., CRC Press, 2017.

[14] S. Davies, K.J. Packer, Pore-size distributions from nuclear magnetic resonance spin-lattice relaxation measurements of fluid-saturated porous solids. I. Theory and simulation, J. Appl. Phys. 67 (1990) 3163–3170. https://doi.org/10.1063/1.345395.

[15] D.P. Gallegos, K. Munn, D.M. Smith, D.L. Stermer, A NMR technique for the analysis of pore structure: Application to materials with well-defined pore structure, J. Colloid Interface Sci. 119 (1987) 127–140. https://doi.org/10.1016/0021-9797(87)90251-7.

[16] R.L. Kleinberg, M.A. Horsfield, Transverse relaxation processes in porous sedimentary rock, J. Magn.

Reson. 88 (1990) 9–19. https://doi.org/10.1016/0022-2364(90)90104-H.

[17] R.L. Kleinberg, W.E. Kenyon, P.P. Mitra, Mechanism of NMR Relaxation of Fluids in Rock, J. Magn. Reson. Ser. A. 108 (1994) 206–214. https://doi.org/10.1006/JMRA.1994.1112.

[18] P.J. McDonald, J.-P. Korb, J. Mitchell, L. Monteilhet, Surface relaxation and chemical exchange in hydrating cement pastes: A two-dimensional NMR relaxation study, Phys. Rev. E. 72 (2005) 011409. https://doi.org/10.1103/PhysRevE.72.011409.

[19] L. Monteilhet, J.-P. Korb, J. Mitchell, P.J. McDonald, Observation of exchange of micropore water in cement pastes by two-dimensional T2−T2 nuclear magnetic resonance relaxometry, Phys. Rev. E. 74 (2006) 061404. https://doi.org/10.1103/PhysRevE.74.061404.

[20] Y. Yao, D. Liu, Comparison of low-field NMR and mercury intrusion porosimetry in characterizing pore size distributions of coals, Fuel. 95 (2012) 152–158. https://doi.org/10.1016/j.fuel.2011.12.039.

[21] P.R.J. Connolly, W. Yan, D. Zhang, M. Mahmoud, M. Verrall, M. Lebedev, S. Iglauer, P.J. Metaxas, E.F. May, M.L. Johns, Simulation and experimental measurements of internal magnetic field gradients and NMR transverse relaxation times (T2) in sandstone rocks, J. Pet. Sci. Eng. 175 (2019) 985–997. https://doi.org/10.1016/j.petrol.2019.01.036.

[22] K.R. Brownstein, C.E. Tarr, Importance of classical diffusion in NMR studies of water in biological cells, Phys. Rev. A. 19 (1979) 2446–2453. https://doi.org/10.1103/PhysRevA.19.2446.

[23] J.-P. Korb, Multiscale nuclear magnetic relaxation dispersion of complex liquids in bulk and confinement, Prog. Nucl. Magn. Reson. Spectrosc. 104 (2018) 12–55. https://doi.org/10.1016/J.PNMRS.2017.11.001.

[24] S. Godefroy, J.-P. Korb, M. Fleury, R.G. Bryant, Surface nuclear magnetic relaxation and dynamics of water and oil in macroporous media, Phys. Rev. E. 64 (2001) 021605. https://doi.org/10.1103/PhysRevE.64.021605.

[25] J.P. Korb, S. Godefroy, M. Fleury, Surface nuclear magnetic relaxation and dynamics of water and oil in granular packings and rocks, Magn. Reson. Imaging. 21 (2003) 193–199. https://doi.org/10.1016/S0730-725X(03)00124-3.

[26] P.J. McDonald, J. Mitchell, M. Mulheron, P.S. Aptaker, J.P. Korb, L. Monteilhet, Two-dimensional correlation relaxometry studies of cement pastes performed using a new one-sided NMR magnet, Cem. Concr. Res. 37 (2007) 303–309. https://doi.org/10.1016/j.cemconres.2006.01.013.

[27] A. Plassais, M.-P. Pomiès, N. Lequeux, P. Boch, J.-P. Korb, Micropore size analysis in hydrated cement paste by NMR, Magn. Reson. Imaging. 19 (2001) 493–495. https://doi.org/10.1016/S0730-725X(01)00276-4.

[28] B. Godel, High-resolution X-ray computed tomography and its application to ore deposits: From data acquisition to quantitative three-dimensional measurements with case studies from Ni-Cu-PGE Deposits, in: Econ. Geol., GeoScienceWorld, 2013: pp. 2005–2019. https://doi.org/10.2113/econgeo.108.8.2005.

[29] R.L. Vold, J.S. Waugh, M.P. Klein, D.E. Phelps, Measurement of spin relaxation in complex systems, J. Chem. Phys. 48 (1968) 3833–3834. https://doi.org/10.1063/1.1669699.

[30] J. Keeler, Understanding NMR spectroscopy, Wiley, 2010.

[31] J.D. Wilson, Statistical approach to the solution of first-kind integral equations arising in the study of

materials and their properties, J. Mater. Sci. 27 (1992) 3911–3924. https://doi.org/10.1007/BF00545476.

[32] H.Y. Carr, E.M. Purcell, Effects of Diffusion on Free Precession in Nuclear Magnetic Resonance Experiments, Phys. Rev. 94 (1954) 630–638. https://doi.org/10.1103/PhysRev.94.630.

[33] S. Meiboom, D. Gill, Modified spin-echo method for measuring nuclear relaxation times, Rev. Sci. Instrum. 29 (1958) 688–691. https://doi.org/10.1063/1.1716296.

[34] J. Mitchell, T.C. Chandrasekera, M.L. Johns, L.F. Gladden, E.J. Fordham, Nuclear magnetic resonance relaxation and diffusion in the presence of internal gradients: The effect of magnetic field strength, Phys. Rev. E. 81 (2010) 026101. https://doi.org/10.1103/PhysRevE.81.026101.

[35] A.N. Tikhonov, V.I.A. Arsenin, Solutions of ill-posed problems, SIAM, 1977.

[36] G.H. Golub, M. Heath, G. Wahba, Generalized cross-validation as a method for choosing a good ridge parameter, Technometrics. 21 (1979) 215–223. https://doi.org/10.1080/00401706.1979.10489751.

[37] P.R.J. Connolly, S.J. Vogt, S. Iglauer, E.F. May, M.L. Johns, Capillary trapping quantification in sandstones using NMR relaxometry, Water Resour. Res. 53 (2017) 7917–7932. https://doi.org/10.1002/2017WR020829.

[38] N. Robinson, L.F. Gladden, C. D'Agostino, Exploring catalyst passivation with NMR relaxation, Faraday Discuss. 204 (2017) 439–452. https://doi.org/10.1039/C7FD00098G.

[39] K.G. Hollingsworth, M.L. Johns, Measurement of emulsion droplet sizes using PFG NMR and regularization methods, J. Colloid Interface Sci. 258 (2003) 383–389. https://doi.org/10.1016/S0021-9797(02)00131-5.

[40] J.D. Griffith, A.E. Bayly, M.L. Johns, Evolving micro-structures in drying detergent pastes quantified using NMR, J. Colloid Interface Sci. 315 (2007) 223–229. https://doi.org/10.1016/j.jcis.2007.06.050.

[41] J. Mitchell, L.F. Gladden, T.C. Chandrasekera, E.J. Fordham, Low-field permanent magnets for industrial process and quality control, Prog. Nucl. Magn. Reson. Spectrosc. 76 (2014) 1–60. https://doi.org/10.1016/J.PNMRS.2013.09.001.

[42] A. Valori, P.J. McDonald, K.L. Scrivener, The morphology of C–S–H: Lessons from 1H nuclear magnetic resonance relaxometry, Cem. Concr. Res. 49 (2013) 65–81. https://doi.org/10.1016/j.cemconres.2013.03.011.

[43] M. Wyrzykowski, A.M. Gajewicz-Jaromin, P.J. McDonald, D.J. Dunstan, K.L. Scrivener, P. Lura, Water Redistribution–Microdiffusion in Cement Paste under Mechanical Loading Evidenced by ^{1}H NMR, J. Phys. Chem. C. 123 (2019) 16153–16163. https://doi.org/10.1021/acs.jpcc.9b02436.

[44] A.C.A. Muller, K.L. Scrivener, A reassessment of mercury intrusion porosimetry by comparison with 1H NMR relaxometry, Cem. Concr. Res. 100 (2017) 350–360. https://doi.org/10.1016/j.cemconres.2017.05.024.

[45] R. Schulte Holthausen, M. Raupach, A phenomenological approach on the influence of paramagnetic iron in cement stone on 2D T 1 -T 2 relaxation in single-sided 1 H nuclear magnetic resonance, Cem. Concr. Res. 120 (2019) 279–293. https://doi.org/10.1016/j.cemconres.2019.03.027.

[46] M. Wyrzykowski, P.J. McDonald, K.L. Scrivener, P. Lura, Water Redistribution within the Microstructure of Cementitious Materials due to Temperature Changes Studied with 1H NMR, J. Phys. Chem. C. 121 (2017) 27950–27962. https://doi.org/10.1021/acs.jpcc.7b08141.

[47] J.W. Bullard, H.M. Jennings, R.A. Livingston, A. Nonat, G.W. Scherer, J.S. Schweitzer, K.L. Scrivener, J.J. Thomas, Mechanisms of cement hydration, Cem. Concr. Res. 41 (2011) 1208–1223. https://doi.org/10.1016/j.cemconres.2010.09.011.

[48] P.T. Callaghan, Translational dynamics and magnetic resonance: principles of pulsed gradient spin echo NMR, Oxford University Press, 2011.

[49] J. Boguszynska, M.C.A. Brown, P.J. McDonald, J. Mitchell, M. Mulheron, J. Tritt-Goc, D.A. Verganelakis, Magnetic resonance studies of cement based materials in inhomogeneous magnetic fields, Cem. Concr. Res. 35 (2005) 2033–2040. https://doi.org/10.1016/j.cemconres.2005.06.012.

[50] R.L. Kleinberg, A. Sezginer, D.D. Griffin, M. Fukuhara, Novel NMR apparatus for investigating an external sample, J. Magn. Reson. 97 (1992) 466–485. https://doi.org/10.1016/0022-2364(92)90028-6.

[51] M.S. Spurlin, B.W. Barker, B.D. Cross, C.E. Divine, Nuclear magnetic resonance logging: Example applications of an emerging tool for environmental investigations, Remediat. J. 29 (2019) 63–73. https://doi.org/10.1002/rem.21590.